Zinc Oxide Nanoparticles with Defects**

By *Vladislav Ischenko*, *Sebastian Polarz*,* *Dirk Grote*, *Victorina Stavarache*, *Karin Fink*, and *Matthias Driess**

Dedicated to R. Kniep on the occasion of his 60th birthday

Zinc oxide in the form of nanoscale materials can be regarded as one of the most important semiconductor oxides at present. However, the question of how chemical defects influence the properties of nanoscale zinc oxide materials has seldom been addressed. In this paper, we report on the introduction of defects into nanoscale ZnO, their comprehensive analysis using a combination of techniques (powder X-ray diffraction (PXRD), X-ray absorption spectroscopy/extended X-ray absorption fine structure (XAS/EXAFS), electron paramagnetic resonance (EPR), magic-angle spinning nuclear magnetic resonance (MAS-NMR), Fourier-transform infrared (FTIR), UV-vis, and photoluminescence (PL) spectroscopies coupled with ab-initio calculations), and the investigation of correlations between the different types of defects. It is seen that defect-rich zinc oxide can be obtained under kinetically controlled conditions of ZnO formation. This is realized by the thermolysis of molecular, organometallic precursors in which ZnO is pre-organized on a molecular scale. It is seen that these precursors form ZnO at low temperatures far from thermodynamic equilibrium. The resulting nanocrystalline ZnO is rich in defects. Depending on conditions, ZnO of high microstructural strain, high content of oxygen vacancies, and particular content of heteroatom impurities can be obtained. It is shown how the mentioned defects influence the electronic properties of the semiconductor nanoparticles.

1. Introduction

The reason for the "nano-hype" that, recently, has conquered all disciplines of natural sciences is the observation that properties of materials depend not only on composition but also on morphology (size and shape). For materials with at least one dimension below 50 nm, the contribution of surface energy to total energy becomes more and more significant the smaller the structures get. Just as chemical and physical properties of surfaces differ from those of the bulk, so do those of nanoscale materials. For (semi)conductors, as the particles become smaller an additional effect, the so-called quantum-size effect, influences, in particular, the bandgap size, and consequently the electronic properties of the material.[1–4] Therefore, particular attention has been devoted to the preparation of nanoscale semiconducting materials.[1] Among these, nanoscaled ZnO is of extraordinary importance and a substantial number of papers have been published reporting on ZnO nanostructures.[5] The application of ZnO ranges from catalysis via gas sensing to UV-light emitters, ceramic varistors, transparent high-power electronics, surface acoustic wave devices, and piezoelectric transducers.[6] Of particular interest is also the use of ZnO as a component of composite catalysts,[7–9] for instance for low-pressure methanol synthesis.[10,11] Existing models of methanol synthesis on the ZnO surface and recent theoretical calculations suggest that oxygen vacancies formed on the surface of ZnO crystals may be the active sites for CO (and CO_2) chemisorption when methanol synthesis is initiated.[12–15]

This points to an interesting issue: (some) key properties of ZnO may depend not only on intrinsic properties such as the particular crystal structure, bulk composition, and morphology of the oxide particles, but furthermore on their defect structure as well.

Thus, it is becoming increasingly established that in order to control the functional properties of nanoscale materials it is necessary to control not only their composition and morphology but also their defect structure.[16–19] To understand and ultimately to control the defect content of inorganic nanostructures can be seen as an important goal.

As already indicated for heterogeneous catalysis, oxygen defects are of particular importance in the case of zinc oxide, leading to deviations in the zinc-to-oxygen ratio ($ZnO_{0.99993}$ at 800 °C).[20] "Empty" oxygen sites (oxygen vacancies, V_O^{2+}) are potential wells that can trap either one (V_O^{+}) or two (V_O^{0}) electrons.[21–26] In addition, the occurrence of interstitial zinc atoms is known. The latter are shallow donors while oxygen vacancies create deep levels.

[*] Dr. S. Polarz, Prof. M. Driess, Dr. V. Ischenko
Institute of Chemistry, Technical University of Berlin
Strasse des 17. Juni 135, D-10623 Berlin (Germany)
E-mail: sebastian.polarz@tu-berlin.de; matthias.driess@tu-berlin.de
D. Grote, V. Stavarache, Dr. K. Fink
Ruhr University Bochum
Universitätsstrasse 150, D-44780 Bochum (Germany)

[**] We gratefully acknowledge Professor Wieghardt and Professor Sander for allowing us to use their EPR facilities. We thank Dr. E. Bill for worthwhile discussions and help in EPR spectroscopy. We thank Prof. A. Wieck for granting access to his photoluminescence facilities. K. V. Klementiev is acknowledged for recording XAS/EXAFS spectra.

Bulk extrinsic defects involve the presence of heteroatoms by substitution for zinc. Depending on heteroatom type, they may produce either shallow or deep levels in the bandgap of ZnO. In this respect, studies devoted to n- and p-doping of ZnO with shallow-level impurities are of particular importance.[27] Intrinsically, zinc oxide is a wide-bandgap n-type semiconductor with bandgap energy $E_g = 3.37$ eV. Divalent substitution for Zn in ZnO has been studied with respect to bandgap variation. The introduction of trivalent (group-III or group-V) elements allows variation of free-charge-carrier concentration, forming donors or acceptor levels in ZnO. In particular, the possibility of introducing acceptors, such as N, Ag, and Li, has been extensively investigated, as an approach to the preparation of p-type semiconducting ZnO.

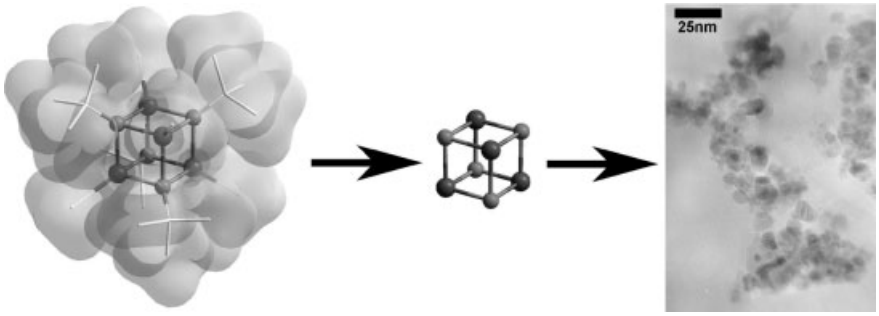

Scheme 1. Schematic representation of the transformation of an organometallic precursor, e.g., $[MeZnO^tBu]_4$ (left), possessing a central Zn_4O_4 motif (middle), to nanocrystalline ZnO obtained at 350 °C (right).

However, although ZnO is such an important material, the role of defects is not yet fully understood. Therefore, we address the following questions in the current contribution:

1. What are suitable preparation approaches for obtaining nanocrystalline model systems with high defect content?
2. What is a comprehensive analytic approach for these defective ZnO samples?
3. What are the consequences of defects for the properties of ZnO?

2. Results and Discussion

2.1. Preparation of ZnO from an Organometallic Precursor

The preceding discussion makes it apparent that the defect structure will strongly depend on the preparation method and the conditions of formation of the ZnO lattice. Thus, routes to ZnO that provide control over the formation rate of the lattice are highly desired. In this respect, organometallic precursors offer several advantages.[28–32] So far, to the best of our knowledge, no comprehensive report exists in the literature on the rational introduction of defects to ZnO.[33,34]

In this contribution, we report the various defects originating from preparing ZnO using molecular organometallic precursors, and the resulting modification of properties due to defects. Our model systems are organometallic alkyl-alkoxyzinc heterocubanes as precursors, which we recently used for the preparation of morphologically controlled ZnO nanoparticles.[35,36] These precursors are "special" because, in a certain sense, ZnO is preorganized on a molecular scale due to the occurrence of a central "Zn_4O_4" motif (Scheme 1). Thermolysis of various alkylzinc alkoxides has been investigated before in the gas phase[35,36] as well as in the solid state.[37] The current contribution reports the solid-state synthesis in a carrier gas containing oxygen to obtain pure, single-phase ZnO samples. From the large variety of alkylzinc alkoxides with different substituents $[R'ZnOR'']_4$ (where $R' = Me$, Et, etc., and $R'' = {}^i$Pr, ^{t}Bu, etc.), we have selected the tetrameric methylzinc *tert*-butoxide $[MeZnO^tBu]_4$. This compound shows the optimum combination of low thermolysis temperature, high stability to oligomerization during storage, and good elimination of organic residues during thermolysis, and is available in large amounts. The thermolysis of $[MeZnO^tBu]_4$ was studied by thermogravimetric analysis (TGA) in an atmosphere containing 20 % O_2 and 80 % Ar and at a heating rate of 10 K min^{-1}. The thermolysis proceeds in two stages (Fig. 1), corresponding to two maxima at ca. 170 °C and 255 °C visible in the DTG (differential thermal gravimetry) curve.

The stepwise transformation of the precursor during thermolysis was studied by Fourier-transform infrared spectroscopy (FTIR) and powder X-ray diffraction (PXRD). IR spectra recorded at different thermolysis temperatures T_D are shown in Figure 2. From the intact precursor up to $T_D = 150$ °C only insignificant changes in IR spectra can be observed. Considering the TG data, this means that the total number of organic leaving groups has decreased, coupled with oligomerization of the single cluster entities. This fits to an increasing contribution of a broad absorption band at ca. 500 cm^{-1}, corresponding to vibration modes observed in bulk ZnO. The complete elimination of initial organic residues is observed at temperatures as low as 250 °C. The ν(C–H) bands at 2800–3000 cm^{-1} disappear completely at this temperature and new broad bands arising at 3400 cm^{-1}, 1400 cm^{-1}, and 1600 cm^{-1} point to the formation of hydroxyl and bidentate carbonate groups. These findings are nicely supported by ^{13}C magic-angle spinning–nuclear magnetic resonance (MAS-NMR) measurements, where signals at $\delta = 181$ ppm were detected. The broad band at 500 cm^{-1}, corresponding to Zn–O vibrations, is already consistent with that observable for bulk ZnO. These observations indicate that even at 250 °C (corresponding to the second step in the TGA curve; Fig. 1) ZnO nanoparticles with significant crystallographic long-range order are formed, a hypothesis also confirmed by PXRD and extended X-ray absorption fine structure (EXAFS) (Fig. 3). Complete thermolysis of $[MeZnO^tBu]_4$ can be reached at 350 °C, if the sample is kept at this temperature for a prolonged time (2 h). However, thermolysis at higher temperatures does not leave a free surface of ZnO behind.

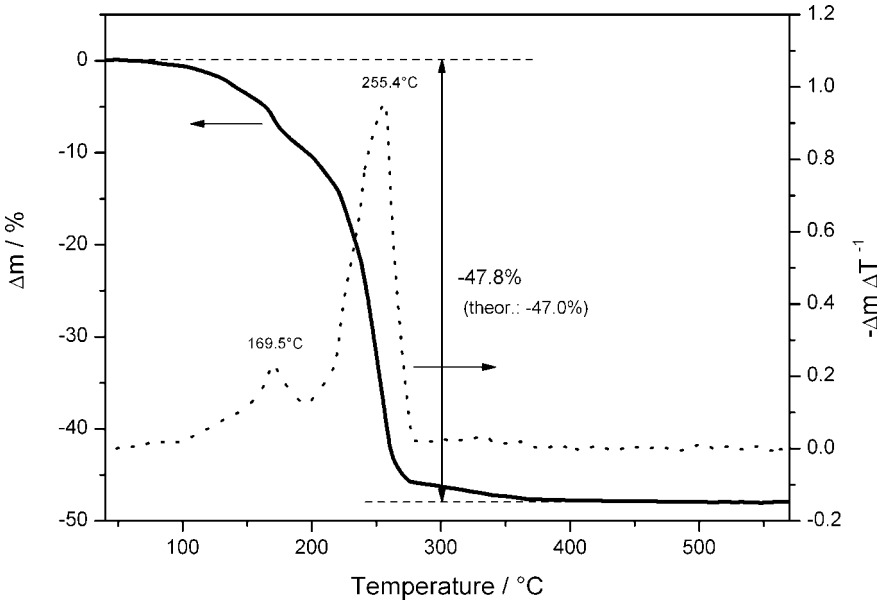

Figure 1. TG analysis of the thermolysis of $[MeZnO^tBu]_4$ (Δm: change in mass).

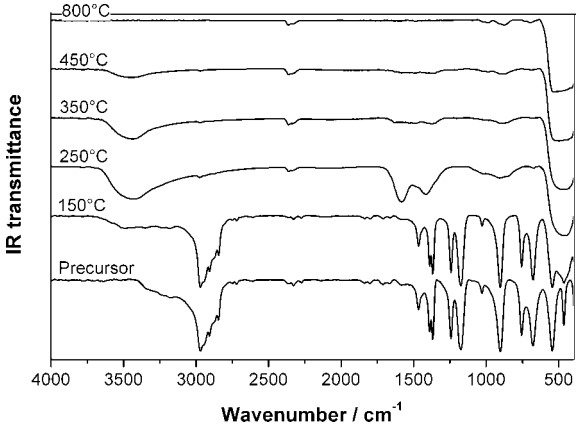

Figure 2. IR spectra of ZnO samples obtained at the indicated thermolysis temperatures.

Hydroxyl groups persist at temperatures above 450 °C. Similarly, the carbonate species can be eliminated only at higher temperatures. The IR spectrum of a sample prepared at 800 °C is finally identical to the spectrum characteristic of pure microcrystalline ZnO.

While IR spectroscopy delivers more information about the leaving organic groups and chemisorbed species, PXRD (Fig. 3a) and complementary X-ray absorption spectroscopy (XAS)/EXAFS (Fig. 3b) enables one to gather insights into the microstructure of the forming Zn–O lattice. With increasing thermolysis temperature, narrowing of the characteristic ZnO diffraction patterns can be observed. The extremely broadened reflections for the sample prepared at 150 °C show the absence of long-range ordering in ZnO due to very small particles, as already indicated by IR. Also in EXAFS (Fig. 3b, line ii) only the second coordination shell of Zn is seen.

2.2. Grain Size, Microstrains, and Lattice Parameters of ZnO

Increasing the temperature leads to particle growth and annealing, as the narrowing of diffraction peaks indicates (Fig. 3a). However, even at higher temperatures (250 °C, Fig. 3b, line iii; 450 °C, Fig. 3b, line iv) significant deviations from bulk ZnO are seen in EXAFS. These deviations cannot be explained by particle-size effects alone, as, for instance, the sample prepared at 450 °C already possesses particles ≈25 nm in diameter. Thus, the deviations in Zn coordination might be additionally interpreted as a first indication of defects. Further information can be obtained from PXDR data. Using the standard procedure of LeBail refinement for experimentally obtained PXRD profiles, it was possible to analyze the contribution of size and strain effects to peak broadening, and by separating the broadening effects for different crystallographic directions (in this case, along and perpendicular to the *c*-axis) to determine the anisotropic components for size and strain parameters. The temperature dependence of grain size is shown in Figure 4a. Considering the results obtained from IR, it seems that the formed ZnO particles are relatively stable as long as organic species cover the interface. Only relatively limited particle growth can be observed between 150 °C (sub-nanometer clusters) and 250 °C (≈7 nm). At higher temperatures (350 °C) this may be accompanied by agglomeration of ≈10 nm large ZnO particles (see the transmission electron microscopy (TEM) image shown in Scheme 1).

Loss of these surface species (Fig. 2) results in significantly stronger particle growth up to ≈70 nm at 600 °C. At this point surface energy has decreased sufficiently, and at 800 °C slower growth to ≈90 nm particles occurs.

The microstrains and deviations of crystal lattice parameters from single-crystal values reflect inherently the imperfections present in the crystal structure, being thus important criteria to characterize the defect structure of the obtained ZnO (Fig. 4).

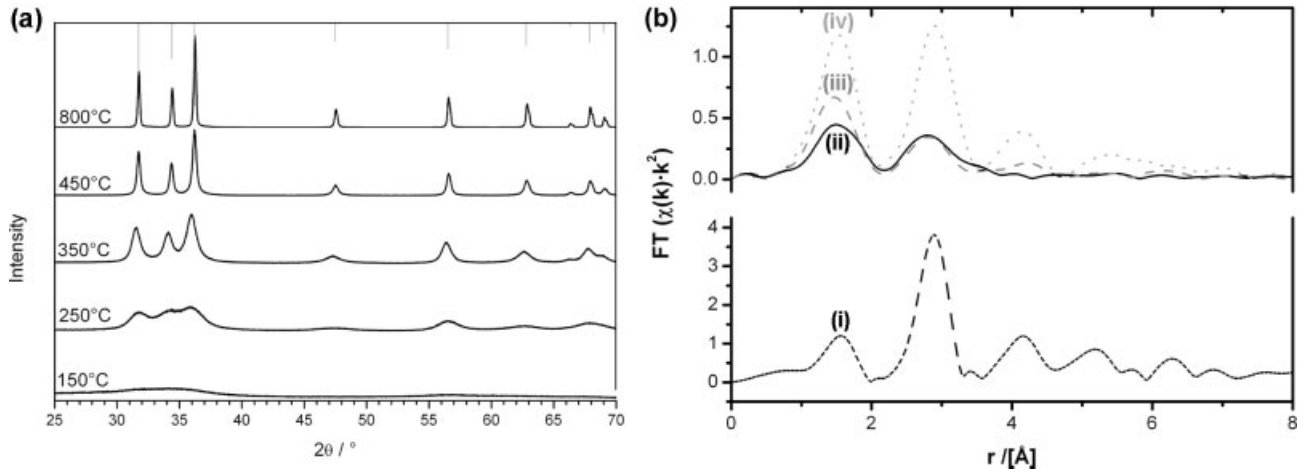

Figure 3. XRD (a) and EXAFS (b) spectra (Zn K-edge) of ZnO samples obtained for different thermolysis temperatures: 150 °C (ii); 250 °C (iii); and 450 °C (iv); i) bulk commercial, macrocrystalline ZnO as a reference.

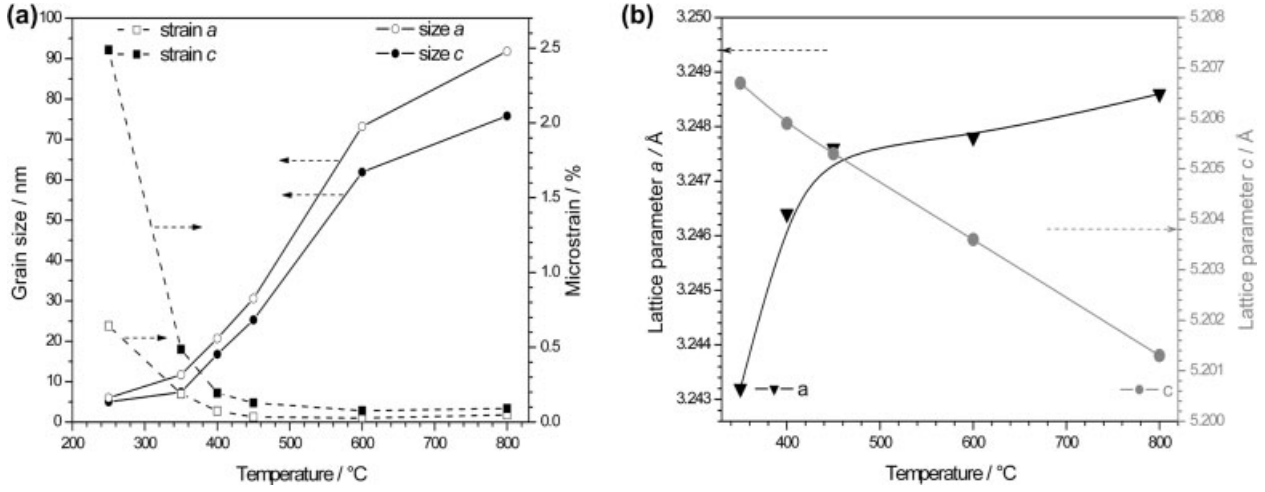

Figure 4. a) Grain size and microstrains in ZnO samples obtained at the indicated thermolysis temperatures from $[MeZnO^tBu]_4$. b) Lattice parameters of ZnO samples obtained at indicated thermolysis temperatures from $[MeZnO^tBu]_4$.

For ZnO prepared at different thermolysis temperatures an almost linear decrease of lattice parameter *c* in the range from 5.207 Å to 5.201 Å (Fig. 4b) can be observed. Interestingly, the final value is below the one expected for the ideal ZnO lattice. At the same time, the lattice parameter *a* increases nonlinearly from 3.243 to 3.249 Å, approaching the corresponding value for the ideal ZnO lattice. This variation of lattice parameters can be understood by taking into account that the increase of the distance along [001] between closely packed atom layers in wurtzite-type structure (e.g., due to high concentration of dislocations) should be compensated by shortening of interatomic distances in the layers perpendicular to it. In any case, the most distorted ZnO structures are obtained for truly nanoscale (<10 nm) particles. The differences in microstrain values along and perpendicular to [001] result from the preferential formation of packing defects in the hexagonal close-packed (hcp) structure along the [001] direction. Owing to this fact, we also observe slight anisotropy of the grain size of ZnO nanoparticles (Fig. 4a), related to slower crystallite growth rate along [001].

2.3. Electronic Properties of Prepared ZnO

So far, it has been shown that it is possible to prepare nanoscale ZnO particles by thermolysis of the particular organometallic precursor used here. The optical properties of semiconductors change significantly as the particle size becomes comparable to the exciton radius (1.8 nm for ZnO).[38] For the materials of this study prepared at higher temperatures, no significant difference in optical properties due to this effect should be expected, compared to bulk ZnO. UV-vis diffuse reflectance spectroscopy confirms that for ZnO prepared above 250 °C the absorption edge is indeed close to 3.2–3.3 eV, which

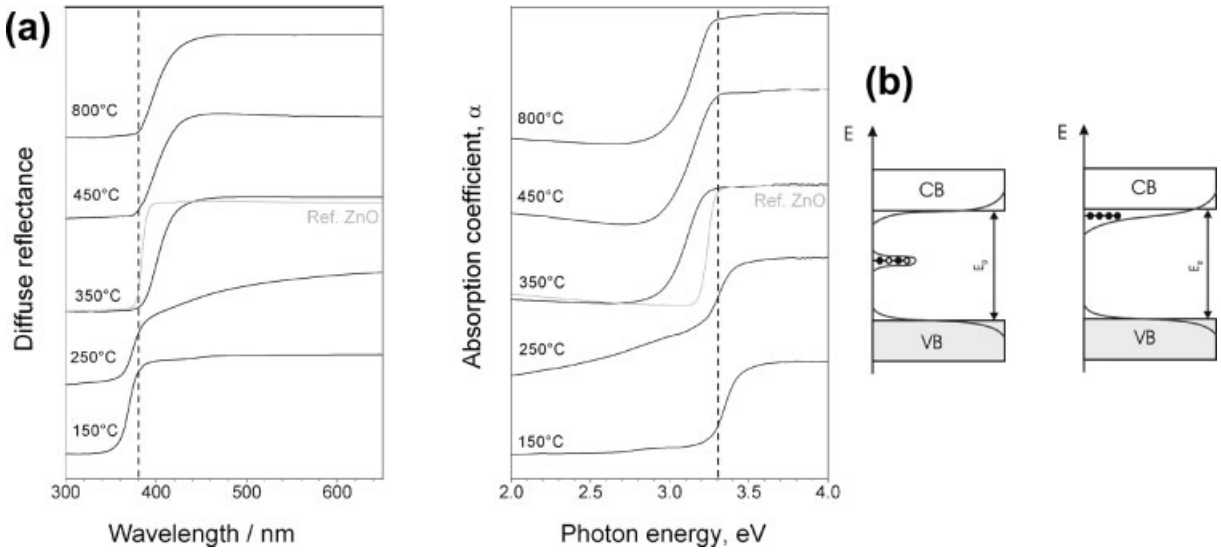

Figure 5. a) UV-vis diffuse reflectance spectra and absorption coefficients of ZnO samples obtained at the indicated thermolysis temperatures from $[MeZnO^tBu]_4$. b) Schematic representation of the effect of impurities and defects on the bandgap (shallow donors, right, and deep levels, left). CB, VB: Conductance and valence bands, respectively.

is usually reported for powder ZnO (Fig. 5). For the samples prepared at $T = 150\,°C$ and 250 °C a considerable blue-shift of the absorption edge up to 3.4 eV can be observed. The related increase of the bandgap of ZnO in this case can be considered as a manifestation of the quantum-size effect. Interestingly, for samples prepared at higher temperatures (larger particles) a characteristic red-shift of the bandgap below the value for the reference is observed. This is most noticeable for the ZnO sample prepared at 350 °C. This red-shift can be explained by the formation of shallow levels inside the bandgap due to impurity atoms present in the lattice (Fig. 5b). Meanwhile, this red-shift usually overlaps with a strong band tailing, which gives a hint of strong disturbances of local symmetry in the ZnO lattice (which is confirmed by EXAFS; Fig. 3b). In principle, these disturbances can be caused either by heteroatoms present in the lattice or by atom-packing defects without inclusion of heteroatoms. The latter defects are expected, however, to be annealed at higher temperatures, so that their contribution to band tailing becomes increasingly small with rising temperature. Even for the sample prepared at 800 °C the observed absorption edge differs significantly from that of reference ZnO. It can be concluded that heteroatoms in the ZnO lattice are indeed responsible for the change in electronic properties.

2.4. Impurities and Oxygen Vacancies

In order to investigate the occurrence of heteroatoms and oxygen vacancies in more detail, electron paramagnetic resonance (EPR) spectroscopy was applied. Surprisingly, because ZnO is expected to be diamagnetic, two types of paramagnetic signals have been observed in the prepared ZnO samples (Fig. 6). The low-field signal with *g*-factor close to the free-electron value ($g = 2.0023$) is generally attributed to an

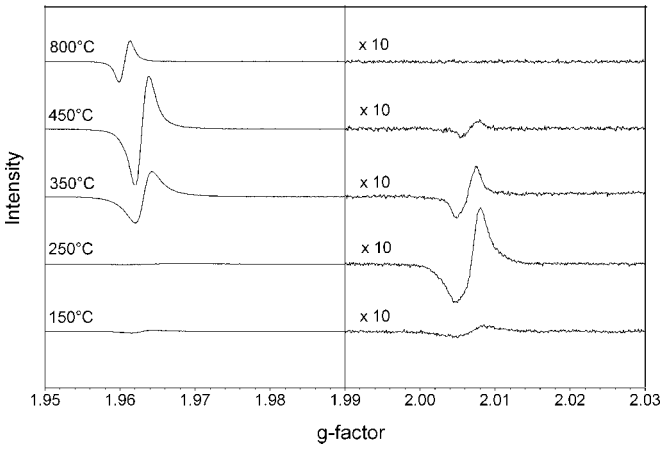

Figure 6. EPR spectra of ZnO samples obtained at the indicated thermolysis temperatures.

unpaired electron trapped on an oxygen vacancy site ($g = 1.9965$, 1.9948;[39] 2.0190;[40] 2.0106[41]). The other, high-field signal at $g \approx 1.96$, which was sometimes also attributed to unpaired electrons trapped on oxygen vacancies, has been reported to result from shallow donor centers such as ionized impurity atoms in the crystal lattice of ZnO.[39,42–46] This is in good agreement with our assumption of impurity atoms in the ZnO lattice.

Furthermore, the experiments indicate that the relative intensity of the first paramagnetic signal in the *g*-factor range between 2.0064 and 2.0069 correlates with the formation rate of the ZnO phase. At a thermolysis temperature around 250 °C—where the thermolysis rate of the precursor is a maximum (Fig. 1)—the low-field paramagnetic signal is most intense. In addition, intentional increase of the thermolysis rate, e.g., by insertion of the precursor in a pre-heated furnace (at 350 °C),

results in up to thirty-times increased intensity of the low-field paramagnetic signal at practically the same *g*-factor value ($g = 2.0059$) in comparison to ZnO obtained by the standard thermolysis procedure (10 K min^{-1} to 350 °C) (Fig. 7).

It must be taken into account that the thermolysis has been followed by 2 h annealing under identical conditions for both samples ($T = 350$ °C in 20 % oxygen atmosphere) allows surface-bound radicals, such as $^{\bullet}OH$ and $^{\bullet}CH_3$, to be excluded as paramagnetic centers responsible for the EPR signal in the obtained ZnO samples.[47,48]

The most abundant bulk point defects in non-stoichiometric ZnO are known to be Zn_i (interstitial zinc) and V_O. Other types of point defects, such as V_{Zn} and O_i may also be thermodynamically stabilized in the ZnO crystal lattice, but at higher oxygen partial pressure. Regarding this fact, it can be concluded that the observed low-field paramagnetic signal in our ZnO samples ($g \approx 2.006$) corresponds to oxygen vacancies with a single trapped electron (V_O^+).

However, the origin of the signal with *g*-factor in the range from 1.9606 to 1.9631 is still unclear. The paramagnetic signal at $g \approx 1.96$ increases in its intensity as the thermolysis temperature is further increased. This observation points to competition between elimination of leaving group atoms and their entrapment in the growing crystal lattice. Considering the chemical composition of the precursor, it is thus expected that primarily carbon atoms can be trapped by the growing crystal lattice and included in the structure as Frenkel- or Schottky-type point defects. Though usually not paramagnetic, carbon atoms can be ionized to other (paramagnetic) oxidation states depending on the position of the Fermi level of ZnO. The presence of carbon in the materials was further confirmed by X-ray photoelectron spectroscopy (XPS) investigations (not shown) and solid-state NMR spectroscopy (see above).

It was already mentioned that the other EPR signal at $g \approx 2.07$ attributed to oxygen vacancies considerably increases for increased thermolysis temperatures. However, increased thermolysis rates lead to the formation of ZnO at even stronger non-equilibrium conditions. The sample prepared at a higher thermolysis rate (Fig. 7a) also contains more carbon as impurity. In this case, an even stronger red-shift of the bandgap can be expected. This is indeed found (Fig. 7b). Different amounts of carbon are introduced as impurity atoms into the ZnO lattice depending on thermolysis conditions.

Taking into account that under equilibrium conditions the concentration of oxygen vacancies in the ZnO crystal lattice is very small (ca. 10^{-5} mol-% at 800 °C) and that a higher content of oxygen vacancies can be reached only under non-equilibrium, kinetically controlled conditions, it is clear that the higher the formation rate of the crystal, the more defective it is. The lowering and disappearance of paramagnetic signals caused by higher thermolysis temperatures (Fig. 6) is, in turn, connected with the well-known phenomenon of defect annealing, resulting in equilibration of the crystal lattice, an argumentation which is nicely supported by the investigations conducted by XRD (Figs. 3,4). Nevertheless, especially at elevated temperatures, the occurrence of stable oxygen vacancies is surprising because the samples were prepared in oxygen-containing atmosphere (see Experimental sect.). Therefore, the idea that a correlation between oxygen vacancies and doping of the ZnO lattice with impurity atoms may exist is straightforward. Taking into account that carbon tends to be trigonal-planar coordinated with oxygen (consider the carbonate anion), one may expect that substitutional carbon, if present, would be next to an oxygen vacancy in the ZnO lattice. So, the effect of oxygen vacancy stabilization through defect-pair formation may be suggested. Therefore, the question arises as to what effects impurities other than carbon have.

It has been demonstrated in the literature that the paramagnetic signal at $g \approx 1.96$ appears often owing to shallow donor impurities in ZnO (e.g., Al, Ga, In),[42–46] with the *g*-factor value being practically independent of the type of impurity. To confirm our hypothesis, pure microcrystalline ZnO (Merck) has been intentionally doped with elemental Zn by annealing it at 850 °C for 30 min in Zn vapor. As a result, the appearance

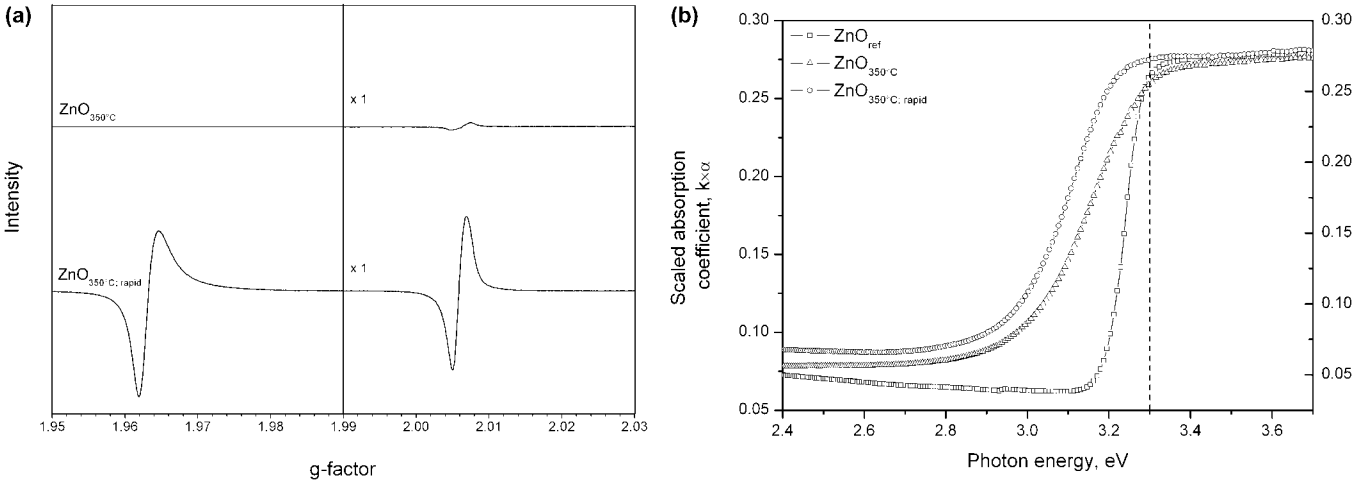

Figure 7. EPR spectra (a) and UV-vis spectra (b) of ZnO samples obtained by thermolysis of $[MeZnO^tBu]_4$ with a heating rate of 5 K min^{-1} to 350 °C and obtained by rapid thermolysis of the same precursor. The UV-vis spectrum of the reference ZnO sample is also given.

of the paramagnetic signal at $g \approx 1.96$ (Fig. 8ii) is observed. Also, if microcrystalline ZnO is heated under vacuum (10^{-2} mbar; 1 mbar = 100 Pa) at 850 °C for 2 h, this paramagnetic signal appears as well (Fig. 8iii). The low-field signal is not observed in either case, confirming the previous result that the signal at the *g*-factor value close to 2.00 appears only at lower temperatures, and that at higher temperatures the related defects are readily annealed. So, increasing the content of Zn over the stoichiometric value in well-crystallized ZnO leads rather to the formation of ZnO with an increased amount of interstitial Zn, instead of high oxygen-vacancy content. This observation is not in accordance with the theoretically predicted prevailing concentration of oxygen vacancies over interstitial zinc atoms in ZnO at higher zinc partial pressure.[20]

It is interesting to note that, in agreement with our study, the paramagnetic signal has been reported to appear at *g*-factor values close to 1.96 even if quite different heteroatoms are introduced into the ZnO lattice. This implies that for different heteroatoms the associated unpaired electron should have the same contribution of orbital angular momentum to orbit–spin interaction to give the same energy splitting in a magnetic field due to the Zeeman effect. As the orbital angular momentum of the electron depends on its wavefunction form, this would also mean that the total energy of the unpaired electron should be practically the same for quite different heteroatoms. We suggest that this non-trivial situation may be similar to the well-known phenomenon of exciton bonding in semiconductors.

Taking into account that coulomb interaction is reciprocal to the distance, the difference in potential energy of the electron caused by different effective charge on the nuclei can be evened out if the electron is only weakly bound to the atom and possesses a rather large Bohr radius (the exciton radius is 18 Å in ZnO).[38] We suppose that the EPR signal at $g \approx 1.96$ may be due to one electron being weakly bound to ionized impurity atoms. This means, in other words, that the electron from a shallow donor level can, in some cases, be not completely delocalized into the conduction band, but stays weakly bound to the original atoms, and behaves much like an electron in a hydrogen-like atom with a large Bohr radius.

To support this hypothesis we have studied the change of EPR spectra of the pure reference ZnO powder under illumination with UV light. The used reference ZnO shows no paramagnetic signal without illumination. The illumination with UV light is expected to produce excitons and, once bound, the exciton (binding energy about 60 meV in ZnO)[38] would give rise to a paramagnetic signal at $g \approx 1.96$ if this signal is indeed related to weakly bound electrons as we suppose. The results of this experiment are shown in Figure 9. The EPR signal at $g \approx 1.96$ appears during illumination with UV light and therefore confirms our hypothesis. In addition, these experiments are clear proof that the signal at $g \approx 1.96$ is not related to oxygen vacancies.

2.5. Photoluminescence and Oxygen Vacancies

According to recent reports in the literature, oxygen vacancies manifest themselves also by the so-called "green" luminescence of ZnO at $\lambda \approx 550$ nm due to the formation of deep levels in the bandgap (Fig. 5b).[20] Consequently, the samples prepared in this study were also investigated by photoluminescence (PL) spectroscopy. The results are shown in Figure 10. Comparison of the EPR data (Fig. 6) with the PL data (Fig. 10) shows that the formation of oxygen vacancies in ZnO is indeed more complicated. There is no direct relation between the EPR signal at $g \approx 2.00$ and the "green" luminescence in PL spectra. Although the samples prepared at 150 °C and 250 °C (most intense EPR signal at $g \approx 2.00$) do show slight "green" luminescence, no luminescence is observed for the samples prepared between 250 °C and 800 °C. Following this observation one can suggest that the EPR signal at $g \approx 2.00$ and the luminescence at $\lambda \approx 550$ nm ($E \approx 2.25$ eV) might not be related to the same point defects, such as oxygen vacancies. It is also interesting that the nanocrystalline ZnO samples prepared here show generally no UV luminescence. This indicates that in these samples the recombination of exciton pairs takes place rather on non-radiative recombination centers, such as dislocations, low-angle intergrain boundaries, and inhomogeneously distributed impurity atoms in the lattice. The same observation has been reported for ZnO polycrystalline films studied by cathodoluminescence.[49] In accordance with these literature data, in our ZnO samples some UV and "green" luminescence is observed only after annealing of the majority of defects at temperatures as high as 800 °C. This result is an additional illustration that the sum

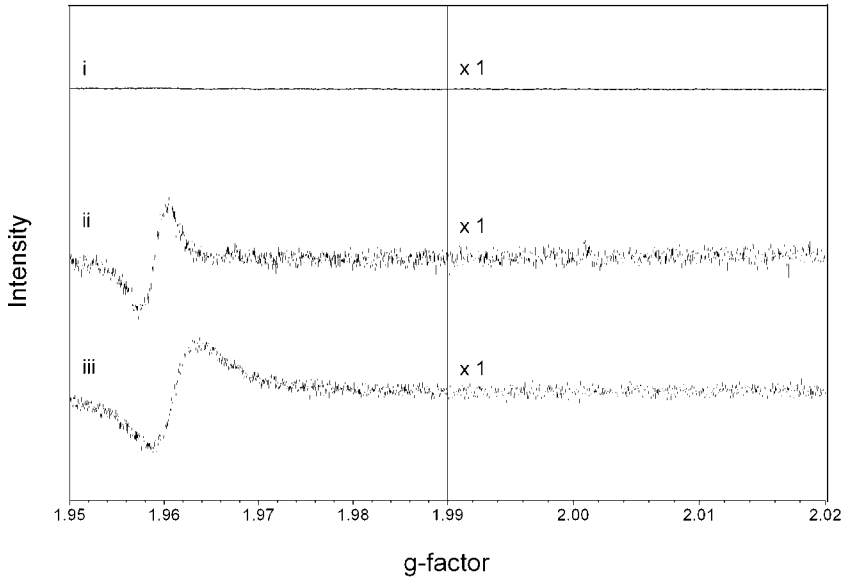

Figure 8. EPR spectra of I) microcrystalline ZnO (Merck) as is, ii) annealed at 850 °C in Zn vapor for 30 min, and iii) annealed at 850 °C under vacuum for 2 h.

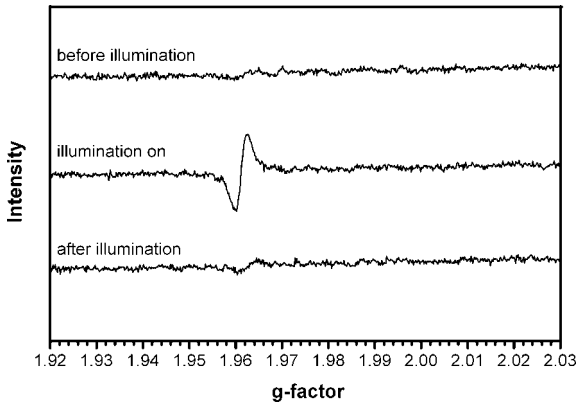

Figure 9. EPR spectra of reference ZnO before, during, and after illumination with UV light.

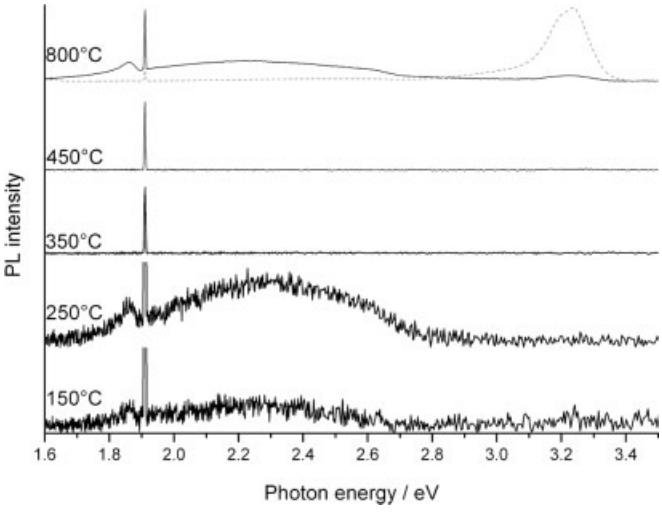

Figure 10. PL spectra of ZnO samples obtained at the indicated thermolysis temperatures from $[MeZnO^tBu]_4$. The data for the reference ZnO sample are represented by the dashed line.

of defects introduced by the kinetically controlled, low-temperature preparation of ZnO from organometallic precursors changes the optical properties of the resulting nanoparticles significantly. In this context, the intentional introduction of additional impurities has already been discussed previously. The "green" luminescence at $\lambda \approx 550$ nm for samples doped with carbon or silicon (spectra not shown) is not very pronounced even in cases when the concentration of oxygen vacancies as shown by EPR (signal at $g \approx 2.00$, Figs. 6,7) is rather high.

As shown and discussed above, the PL (in both UV and visible ranges) in highly defective ZnO samples is readily quenched due to non-radiative recombination. So, it is not easy to separate the effects produced by different types of defects from each other. However, this quenching is not observed for the well-crystallized reference ZnO. In this context, it is interesting to study the effect on PL properties of zinc oxide due solely to doping with excessive Zn. The results are presented in Figure 11. A considerable increase of the "green" luminescence intensity is observed if excessive Zn is introduced into the ZnO lattice. As was shown above (Fig. 8), these Zn-doped ZnO samples manifest no paramagnetic signal related to singly charged oxygen vacancies ($g \approx 2.00$), but only that which we attributed to the shallow donor (interstitial Zn). This observation confirms that there is no direct correlation between "green" luminescence intensity and oxygen-vacancy content in ZnO.

This hypothesis is further supported by quantum-mechanical calculations. Thus, the absorption and emission spectra of an oxygen vacancy V_O were investigated by ab-initio calculations with an embedded cluster approach. The details of the calculations are given by Fink.[50] The ab-initio part of the cluster consists of the oxygen vacancy, the four neighboring Zn ions, the next oxygen shell (12 oxygen ions), and all Zn ions directly bound to these oxygen ions. The cluster was embedded in an extended point charge field consisting of 2+ and 2– charges for Zn and O ions, respectively, to represent the long-range electrostatic interactions in bulk ZnO. In the interface region between the cluster and the point charge field the positive Zn ions were described by a large core Zn pseudopotential to prevent the electrons moving to the positive charges in the point charge field. The excited states were obtained by a state average complete active space self-consistent field (CASSCF) calculation.[51] The geometric relaxation of the Zn ions next to the vacancy was considered for the different states and we included dynamic correlations by the multiconfiguration coupled electron pair approximation (MCCEPA) method.[52] For the blue absorption of the $V_O^\bullet$ center we obtained an absorption energy of 3.19 ± 0.3 eV. The calculated oscillator strength of 0.38 is quite high, but it has to be considered that the number of O vacancies in the crystal is small.

The very good agreement with the experimental value of 2.95–3.03 eV[53] (Fig. 7) is a sign of the satisfactory accuracy of our calculations. Therefore, we applied the described method for the determination of the expected wavelength of luminescence caused by oxygen vacancy sites. One of the possible mechanisms for the PL at 2.38–2.45 eV that was discussed in the literature is an emission from an excited $^3T_2$ state of the

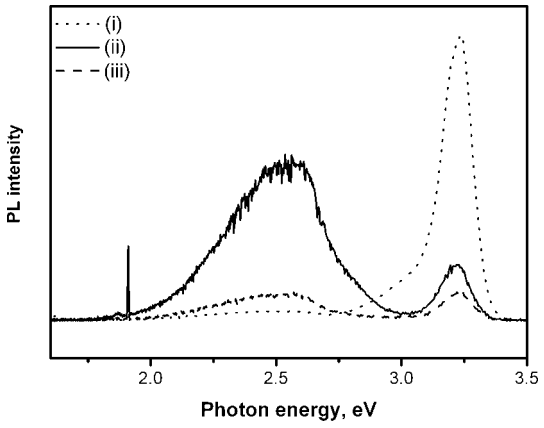

Figure 11. PL spectra of pure and Zn-doped ZnO samples: i) microcrystalline ZnO (Merck) as received, ii) annealed at 850 °C in Zn vapor for 30 min, and iii) annealed at 850 °C under vacuum for 2 h.

neutral V_O^0 center to the $^1A_1$ ground state. The triplet state could be reached by spin–orbit coupling with an excited singlet state. This mechanism is proposed for example by Leiter et al.[54] The authors proved the existence of a triplet state by optical detection of magnetic resonance (ODMR) measurements. In our calculations, we obtained an energy difference of 2.73 ± 0.3 eV between the excited $^3T_2$ state and the $^1A_1$ ground state of the neutral V_O^0 center at the equilibrium geometry of the triplet, which differs significantly from the experimental values (Figs. 10,11). It is expected that calculations on the latter transition should be even more accurate than for the blue absorption, because the relaxation of the geometry as well as the dynamic correlation energy are much smaller in this case. Therefore, from the viewpoint of ab initio calculations as well, one has to assume that the green PL is not caused by the $^3T_2$ to $^1A_1$ transition of the neutral V_O^0 center. However, the energy difference from the calculated transition to the experimentally observed transition is sufficiently small that this transition cannot be excluded for sure as the origin of the green PL solely by quantum mechanical calculations.

3. Conclusions

We can now answer the questions raised in the introductory section of this paper as follows.

1. Highly defective, nanocrystalline ZnO can be prepared far from thermodynamic equilibrium. This assumption is in good agreement with recent theoretical calculations of the thermodynamic stability of oxygen vacancy sites in ZnO.[55] Formation of ZnO under non-equilibrium conditions was achieved by an organometallic precursor possessing a Zn_4O_4 cluster as the smallest building block for ZnO pre-organized on the molecular scale. A further advantage of this precursor is that formation of ZnO is possible at low temperatures. This enables ZnO to be obtained in the form of small clusters as a step towards nanocrystalline materials. The formation of the ZnO lattice is kinetically controlled and this allows defects to be introduced. However, it is not possible to "adjust" one defect type independently without changing other materials parameters (e.g., particle size).

2. In the case of ZnO, we were able to identify three types of defects that are related to each other: microstructural strain, presence of impurities in the ZnO lattice, and oxygen vacancies. A reliable analysis of the defect structure of ZnO requires, according to our experience summarized in this paper, always a combination of several analytical techniques. Although with regard to composition and morphology some samples were very similar, it was still seen that every ZnO sample is different, depending on how it was prepared.

3. The presence of defects had a significant impact on the electronic properties of the materials. This was seen from UV-vis spectroscopy but even more from PL spectroscopy. The luminescence properties, being very important for many applications of ZnO, can be quantitatively quenched by the occurrence of defects (oxygen defects), or enhanced (interstitial zinc).

What becomes obvious from the findings reported here is that control of morphology (size and shape) and composition (ZnO) is not sufficient in order to achieve control over properties of materials in the nanoscale. Bottom–up techniques introduce defects, and these defects can strongly influence the properties of the materials too. Thus, controlling materials properties, which is the highest goal of contemporary nanotechnology, needs to involve the control of defects as well.

4. Experimental

Sample Preparation: Nanocrystalline ZnO was prepared by thermolysis of methylzinc *tert*-butoxide, $[MeZnO^tBu]_4$ (for the preparation procedure of the latter see elsewhere [56]). The thermolysis was conducted in a quartz tube reactor at different temperatures in the range from 150 °C to 850 °C. A gas mixture flow of 80 sccm (sccm: standard cubic centimeters per minute) argon and 20 sccm oxygen was used unless otherwise indicated. The heating rate toward the final temperature was 5 K min^{-1}, with 2 h heating time after reaching the temperature. Commercially available microcrystalline ZnO (Merck, 99.9+ %) was used as a reference material for comparison with ZnO prepared by thermolysis of $[MeZnO^tBu]_4$.

Analytical Methods: Thermogravimetric analyses (differential thermal analysis (DTA), thermogravimetry (TG)) of the precursor were carried out with a thermogravimetric setup from Rubotherm. X-ray diffractograms were recorded with a Bruker-AXS D8 Advance instrument using Cu Kα radiation ($\lambda = 1.5418$ Å) and a position-sensitive detector (PSD) diffractometer using Cu Kα radiation in the 2θ range from 25° to 85° with 0.015° step size. Crystallite size and microstrain parameters were determined by full-profile LeBail fit of the experimental XRD pattern with subsequent decomposition of the reflection profile into Gaussian and Lorentzian parts, taking into account instrumental contribution to peak broadening. X-band EPR spectra were recorded with a Bruker Elexsys E500 EPR spectrometer with an ER077R magnet (75 mm pole cap distance), and an ER047 XG-T microwave bridge. The irradiation of the samples was performed by an Oriel high-pressure mercury lamp. Cylindrical quartz tube containers were used to insert the samples into the microwave cavity. FTIR spectra were taken with a Bruker Vector 22 spectrometer (KBr pellets). UV-vis spectra were recorded using a Perkin–Elmer Lambda 20 spectrometer equipped with a reflecting sphere, Labsphere RSA-PE-20. For PL measurements, a UV HeCd laser with 325 nm wavelength and about 36 mW power was used as an excitation source. All the measurements were performed at room temperature (300 K). The samples were fixed on a finger cryostat on the front side. The cryostat was mounted on an *xyz*-table, which permitted the sample to be moved in three directions. This *xyz*-table offers the possibility of moving the sample to the intersection point of the laser beam and the optical axis. From the laser, the light was periodically cut with a chopper and reached the sample via a mirror. The standard frequency was 133 Hz. Between chopper and mirror the light could be controlled by a remote control. Through the second lens the light was focused on the entrance of the monochromator (Jobin Yvon Spex 500M). From the monochromator the light was detected by a Si photodiode detector and converted into a signal that was measured with a lock-in amplifier. The monochromator control and the data processing were carried out with a computer.

The absorption edges of Cu and Zn at 8979.0 and 9659 eV, respectively, were measured at the Hasylab E4 station (Hamburg, Germany). This beam line was equipped with a Si(111) double-crystal monochromator that was used to detune the beam to 50 % of the maximum intensity in order to exclude higher harmonics present in the X-ray beam. Immediately preceding the recording of XAS spectra, samples were cooled rapidly to liquid nitrogen temperature. The spectra $\mu(k)$ were measured in transmission mode using ionization chambers. A metal foil (between the second and the third ionization chambers) was measured at the same time for energy calibration purposes. Data treatment was

carried out using the software package VIPER35. For background subtraction a Victoreen polynomial was fitted to the pre-edge region. A smooth atomic background $\mu_0(k)$ was evaluated using smoothed cubic splines. The radial distribution function FT[$k^2\chi(k)$] was obtained by Fourier transformation of the k^2-weighted experimental function $\chi(k) = (\mu(k) - \mu_0(k))/\mu_0(k)$ multiplied by a Bessel window. Duplicate spectra were recorded to ensure data reproducibility.

Received: February 9, 2005
Final version: July 26, 2005

[1] A. P. Alivisatos, *Science* **1996**, *271*, 933.
[2] A. P. Alivisatos, *NATO Sci. Ser., Ser. C* **1999**, *519*, 405.
[3] A. P. Alivisatos, *Endeavour* **1997**, *21*, 56.
[4] A. P. Alivisatos, *MRS Bull.* **1995**, *20*, 23.
[5] E. A. Meulenkamp, *J. Phys. Chem. B* **1998**, *102*, 5566.
[6] S. J. Pearton, D. P. Norton, K. Ip, Y. W. Heo, T. Steiner, *J. Vac. Sci. Technol.* **2004**, *22*, 932.
[7] K. C. Waugh, *Catal. Today* **1992**, *15*, 51.
[8] L. Lloyd, D. E. Ridler, M. V. Twigg, in *Catalyst Handbook* (Ed: M. V. Twigg), Wolfe, London **1989**.
[9] J. Agrell, B. Lindström, L. J. Pettersson, S. G. Järas, in *Catalysis—Specialist Periodical Reports*, Vol. 16 (Ed: J. J. Spivey), Royal Society of Chemistry, Cambridge, UK **2002**, p. 67.
[10] M. Kurtz, N. Bauer, H. Wilmer, O. Hinrichsen, M. Muhler, *Chem. Ing. Tech.* **2004**, *76*, 42.
[11] B. A. Peppley, J. C. Amphlett, L. M. Kearns, R. F. Mann, *Appl. Catal. A* **1999**, *179*, 21.
[12] J. C. Lavalley, J. Saussey, T. Rais, *J. Mol. Catal.* **1982**, *17*, 289.
[13] H. H. Kung, *Catal. Rev.—Sci. Eng.* **1980**, *22*, 235.
[14] S. A. French, A. A. Sokol, S. T. Bromley, C. R. A. Catlow, S. C. Rogers, F. King, P. Sherwood, *Angew. Chem. Int. Ed.* **2001**, *40*, 4437.
[15] S. A. French, A. A. Sokol, S. T. Bromley, C. R. A. Catlow, P. Sherwood, *Top. Catal.* **2003**, *24*, 161.
[16] P. Lindan, E. Duplock, C. Zhang, M. Thomas, R. Chatten, A. Chadwick, *Dalton Trans.* **2004**, 3076.
[17] J. Maier, *Phys. Chem. Chem. Phys.* **2003**, *5*, 2164.
[18] J. C. H. Spence, *Science* **2003**, *299*, 839.
[19] P. Knauth, *J. Solid State Electrochem.* **2002**, *6*, 165.
[20] A. F. Kohan, G. Ceder, D. Morgan, C. G. Van de Walle, *Phys. Rev. B* **2000**, *61*, 15 019.
[21] J. M. Smith, W. E. Vehse, *Phys. Lett. A* **1970**, *31*, 147.
[22] K. Vanheusden, W. L. Warren, C. H. Seager, D. R. Tallant, J. A. Voigt, B. E. Gnade, *J. Appl. Phys.* **1996**, *79*, 7983.
[23] W. E. Carlos, E. R. Glaser, D. C. Look, *Physica B* **2001**, *308*, 976.
[24] B. X. Lin, Z. X. Fu, Y. B. Jia, *Appl. Phys. Lett.* **2001**, *79*, 943.
[25] F. Oba, S. R. Nishitani, S. Isotani, H. Adachi, I. Tanaka, *J. Appl. Phys.* **2001**, *90*, 824.
[26] X. L. Wu, G. G. Siu, C. L. Fu, H. C. Ong, *Appl. Phys. Lett.* **2001**, *78*, 2285.
[27] D. C. Look, D. C. Reynolds, C. W. Litton, R. L. Jones, D. B. Eason, G. Cantwell, *Appl. Phys. Lett.* **2002**, *81*, 1830.
[28] H. Kleinwechter, C. Janzen, J. Knipping, H. Wiggers, P. Roth, *J. Mater. Sci.* **2002**, *37*, 4349.
[29] N. Audebrand, J. P. Auffredic, D. Louer, *Chem. Mater.* **1998**, *10*, 2450.
[30] F. Rataboul, C. Nayral, M. J. Casanove, A. Maisonnat, B. Chaudret, *J. Organomet. Chem.* **2002**, *643*, 307.
[31] J. J. Robbins, C. Fry, C. A. Wolden, *J. Cryst. Growth* **2004**, *263*, 283.
[32] H. Sato, T. Minami, T. Miyata, S. Takata, M. Ishii, *Thin Solid Films* **1994**, *246*, 65.
[33] R. J. D. Tilley, *Defect Crystal Chemistry and Its Applications*, Chapman and Hall, London **1987**.
[34] A. M. Stoneham, *Theory of Defects in Solids*, Oxford University Press, Oxford, UK **2001**.
[35] S. Polarz, A. Roy, M. Merz, S. Halm, D. Schröder, L. Scheider, G. Bacher, F. E. Kruis, M. Driess, *Small* **2005**, *1*, 540.
[36] M. Driess, K. Merz, R. Schoenen, S. Rabe, F. E. Kruis, A. Roy, A. Birkner, *C. R. Chim.* **2003**, *6*, 273.
[37] E. C. Ashby, G. F. Willard, A. B. Goel, *J. Org. Chem.* **1979**, *44*, 1221.
[38] *Landolt–Börnstein New Series*, *Group III, Vol. 41B.*
[39] N. G. Kakazev, T. V. Sreckovic, M. M. Ristic, *J. Mater. Sci.* **1997**, *32*, 4619.
[40] B. Yu, C. Zhu, F. Gan, Y. Huang, *Mater. Lett.* **1998**, *33*, 247.
[41] L. Jing, Z. Xu, J. Shang, X. Sun, W. Cai, H. Guo, *Mater. Sci. Eng. A* **2002**, *322*, 356.
[42] J. Schneider, A. Rauber, *Z. Naturforsch. A* **1961**, *16*, 712.
[43] M. Schulz, *Phys. Status Solidi A* **1975**, *27*, K5.
[44] D. Block, A. Herve, R. T. Cox, *Phys. Rev. B* **1982**, *25*, 6049.
[45] C. Gonzales, D. Block, R. T. Cox, A. Herve, *J. Cryst. Growth* **1982**, *59*, 357.
[46] N. Y. Garces, L. Wang, L. Bai, N. C. Giles, L. E. Halliburton, G. Cantwell, *Appl. Phys. Lett.* **2002**, *81*, 622.
[47] M. Anpo, T. Shima, Y. Kubokawa, *Chem. Lett.* **1985**, 1799.
[48] O. I. Micic, Y. Zhang, K. R. Cromack, A. D. Trifunac, M. C. Thurnauer, *J. Phys. Chem.* **1993**, *97*, 7277.
[49] F. Bertram, D. Forster, J. Christen, N. Oleynik, A. Dadgar, A. Krost, *Appl. Phys. Lett.* **2004**, *85*, 1976.
[50] K. Fink, *Phys. Chem. Chem. Phys.* **2005**, *7*, 2999.
[51] U. Meier, V. Staemmler, *Theor. Chim. Acta* **1989**, *76*, 95.
[52] R. Fink, V. Staemmler, *Theor. Chim. Acta* **1993**, *87*, 129.
[53] W. E. Vehse, W. A. Sibley, F. J. Keller, Y. Chen, *Phys. Rev.* **1968**, *167*, 828.
[54] F. Leiter, H. Alves, D. Pfisterer, N. G. Romanov, D. M. Hofmann, B. K. Meyer, *Physica B* **2003**, *340*, 201.
[55] B. Meyer, *Phys. Rev. B* **2004**, *69,* 045 416.
[56] W. A. Herrmann, S. Bogdanovic, J. Behm, M. Denk, *J. Organomet. Chem.* **1992**, *430*, C33.